International Journal of Automotive Technology, Vol. 19, No. 6, pp. 949–957 (2018)
DOI 10.1007/s12239–018–0092–2

pISSN 1229–9138/ eISSN 1976–3832

AERODYNAMIC DESIGN OF A SOLAR ROAD VEHICLE

Ljubomir Majdandžić[1)], Dalibor Buljić[1)], Andrija Buljac[2)] and Hrvoje Kozmar[2)*]

[1)]Faculty of Electrical Engineering, Josip Juraj Strossmayer University of Osijek, 31000 Osijek, Croatia
[2)]Faculty of Mechanical Engineering and Naval Architecture, University of Zagreb, 10000 Zagreb, Croatia

(Received 4 May 2017; Revised 13 March 2018; Accepted 26 July 2018)

ABSTRACT–Solar road vehicles have very specific design requirements. This makes their aerodynamic characteristics quite different from classic sedan vehicles. In the present study, the computational model of a typical solar road vehicle was developed to investigate its aerodynamic forces and flow characteristics. Computations were performed assuming the steady viscous flow and using the Reynolds-averaged Navier Stokes equations along with the k-ω turbulence model. The obtained results indicate some important findings that are commonly not present for classic sedan vehicles. In particular, a contribution of the viscous drag force to the overall drag force is considerably larger (41 %) than it is the case for the standard passenger road vehicles, where the form drag force dominates over the viscous drag force. Surface pressure distribution patterns indicate a favorable aerodynamic design of this vehicle. In particular, larger pressure coefficients on the top of the vehicle body as compared to the bottom surface contribute to increasing a downforce and thus the vehicle traction. The airfoil-shaped cross-section of the designed cockpit canopy has favorable properties with respect to reduction of the aerodynamic drag force.

KEY WORDS : Solar electric vehicle, Aerodynamic design and forces, Computational model, Reynolds-averaged Navier-Stokes equations, k-ω turbulence model

1. INTRODUCTION

Aerodynamic characteristics of classic sedan vehicles are generally well known, while the practical limitations of their outer shape with respect to aerodynamic characteristics are properly addressed in the literature. Even though various technical solutions are applied to optimize their fuel consumption (Sharma *et al*., 2013), the large contribution of transportation industry to overall carbon emissions makes the application of renewable energy sources for transportation strongly required (Amann, 1994). Consequently, an intense development of vehicles powered by renewable energy sources is observed, e.g. (Doig and Beves, 2014; Rao *et al*., 2009), whereas solar energy proves to be particularly suitable for those purposes (Birnie, 2016; Saber and Venayagamoorthy, 2011). Due to specific requirements of solar cells with respect to necessary area for their placement and proper orientation towards the sun, these vehicles are characterized by significantly different design when compared to classic sedan vehicles. While some recent studies deal with this issue (Doig and Beves, 2014; Taha *et al*., 2011), further efforts are still required to allow for fully understanding the advantages and drawbacks of the aerodynamic design of solar road vehicles.

In order to make renewable energy sources suitable for road vehicles, it is necessary to minimize the overall resistance of the vehicle motion system. One of the main goals is to minimize the aerodynamic drag force, which acts in the direction opposite of the vehicle moving direction, as to increase fuel efficiency of vehicles. This force consists of the form drag force and viscous drag force contributions.

The flow separation in the wake of the generic vehicle blunt body may increase the overall drag force by up to 10 % (Barros *et al*., 2016). The form drag force can be reduced by optimizing the shape of the vehicle body to avoid flow separation (Katz, 1996). The rear body shape of a sedan vehicle can be optimized to decrease the fuel consumption (Song *et al*., 2012). The concept of the vehicle shaped as a fish box proves to be appropriate as relatively low drag coefficients are obtained (Taha *et al*., 2011). Modifications in the engine cooling system at the front of the vehicle can reduce the drag force by 2 % and lift force by 5 % (Khaled *et al*., 2012), whereas cooling of the photovoltaic modules also has to be considered when designing solar vehicle body (Vinnichenko *et al*., 2014). In addition to the form drag force, the viscous drag force occurs due to the air viscosity and the friction between the air and the vehicle surface. It can be reduced by decreasing the overall area of the vehicle parallel to the main flow, as well as by smoothing the vehicle surface.

Various devices are used to decrease the overall air resistance of common sedan vehicles as well. A proper design of a rear diffuser can reduce the aerodynamic drag force of sedan vehicles by up to 4 % (Kang *et al*., 2012).

**Corresponding author.* e-mail: hrvoje.kozmar@fsb.hr

Active flow control by using the microjet arrays favorably influences the aerodynamic drag force (McNally *et al*., 2015).

In the present study, the scope was to computationally investigate aerodynamic characteristics of a typical solar road vehicle with unconventional streamlined body. A particular focus was on the form and viscous contributions to the overall drag force. The study indicates possible effects when optimizing outer body shape of solar road vehicles with respect to their aerodynamic drag force.

2. COMPUTATIONAL SETUP

2.1. Computational Model Description

The studied vehicle is the CROsolar01 of the University of Osijek manufactured in the 2015/2016 academic year, Figure 1. The vehicle is equipped with 6 m^2 of the solar panels with the photovoltaic power of 1.3 kW and the efficiency of 23.9 %. The solar panels are placed on the top surface of the vehicle body and oriented towards the sun. The battery pack with the 5.3 kWh is placed inside the aluminum space frame and covered with the vehicle body. Two electric motors are in-wheel placed with nominal power of 1 kW (maximum power is 2.5 kW) with the efficiency larger than 95 %.

In the computational model of the studied vehicle, fine details of the vehicle geometry such as the rims, suspension parts and electric motors attached to the rear rims were not modeled. They are however considered not to considerably influence the obtained results as they are covered with the vehicle body, while their implementation in the computational model would have unnecesarily increased the complexity of geometrical discretization and computational time. The computational model of the solar vehicle with depicted main parts of the vehicle body is reported in Figure 2.

Figure 1. CROsolar01 prototype vehicle of the University of Osijek.

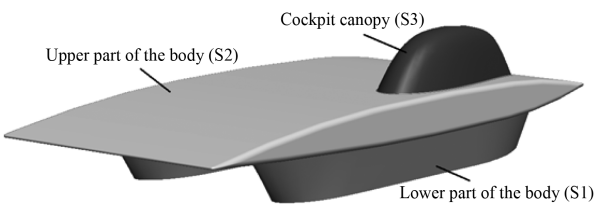

Figure 2. Computational model of the studied CROsolar01 vehicle.

The shape of the solar vehicle body is optimized with respect to the aluminum space frame placed inside the body shell. It can be divided into two lower parts of the vehicle body (S_1 shape), upper part of the vehicle body (S_2 shape), and cockpit canopy (S_3 shape). The two lower parts of the vehicle body cover the chassis and the wheels assembly, while the width of these parts is limited with respect to the necessary space for the driver's seat and the wheels space for maneuvering the vehicle. The middle part of the vehicle body covers the chassis and provides the support for the solar cells. The cockpit canopy used to protect the driver is designed as a sweep feature of the NACA0012 airfoil-shape cross-sections, e.g. (Gregory and O'Reilly, 1973) to minimize the aerodynamic drag force. The vehicle is 4.33 m long and 1.73 m wide, while the height from the ground to the top of the cockpit canopy is 1.05 m.

2.2. Computational Domain

The dimensions of the computational domain were designed to satisfy the requirements for the model blockage of the domain and to obtain the uniform flow at the domain outflow surface. The critical blockage factor is commonly accepted 6 % (West and Apelt, 1982), which is calculated as a ratio of the frontal surface of the model and the frontal surface of the domain (perpendicular to the *x*-axis). The vehicle blockage of the computational domain in this study was 1.75 %, hence it can be adopted that the domain boundaries did not influence the flow around the vehicle, and accordingly no corrections were applied to the results. The main dimensions of the computational domain with respect to the dimensions of the solar vehicle are presented in Figure 3.

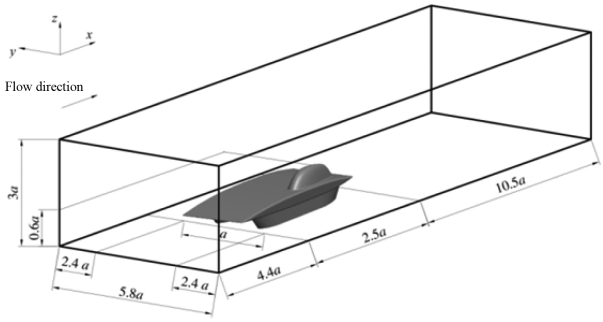

Figure 3. Main dimensions of the computational domain with respect to the dimensions of the model.

Geometrical discretization was carried out using several blocks of the unstructured tetrahedral cells. In the area close to the vehicle body, the 15 mm cells at the vehicle surface expanded with the growth factor of 1.3. In this way, the mesh was finer in the vicinity of the vehicle, hence the

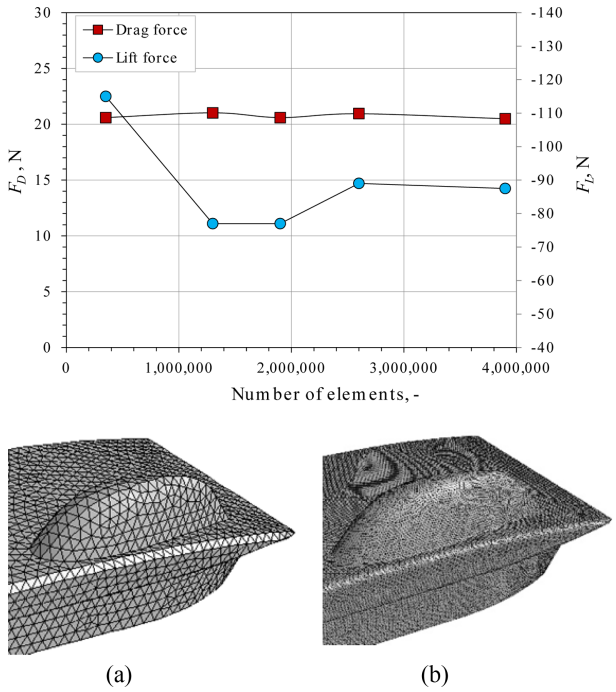

Figure 4. Results for the grid independence test for Re = 3.83 × 10^6: (a) Detail of the coarse mesh with 0.35 M volumes; (b) Detail of the fine mesh with 3.9 M volumes.

distribution of the pressure at the surface was accordingly calculated.

As the body of the vehicle is streamlined, it is important to accurately model the mesh close to the vehicle surface. The size of the first control volume close to the vehicle body was determined based on recommended values of the dimensionless wall distance of the control volume node y^+ from 30 to 60 to allow for reliable results, e.g. (Salim and Cheah, 2009). The results are reported for the geometrical discretization of the computational domain with overall number of control volumes of 2.65 million. Grid independence study indicates that for this density and distribution of control volumes the geometrical discretization negligibly influences the obtained results, Figure 4.

The details of the adopted geometrical discretization of the vehicle body are reported in Figure 5.

Figure 5. Details of the geometrical discretization of the vehicle body.

2.3. Boundary and Initial Conditions

The symmetrical boundary condition (zero-shear slip walls) was applied for the top and lateral surfaces of the computational domain, Figure 3. The bottom surface of the computational domain was simulated as a moving wall without the boundary layer development, and with the translational velocity equal to the freestream flow velocity, as this corresponds to the road conditions (Elofsson and Bannister, 2002; Huminic and Huminic, 2017). This condition is even more important for vehicles with small ground clearance such as in the present study, as potential boundary layer development at the road may interact with the boundary layer at the bottom of the vehicle body (Katz, 1996). The surface of the vehicle was defined as a static wall with the non-slip condition to simulate viscous force effects. The surface roughness of the vehicle body was defined as a hydrodynamically smooth surface because it is made out of the carbon-fibre reinforced plastic that is additionaly painted and polished.

As the wheels of the vehicle are predominantly covered with the S_1 shape and not exposed to the air flow, they were not modelled with the additional rotational velocity.

The influence of Reynolds number on obtained results was studied by performing the computations at different averaged freestream velocities v_∞ at the inlet of the computational domain. The Reynolds number was calculated as $Re = \rho v_\infty L/\mu$, where ρ is air density equal to 1.177 kg/m^3, L = 4.33 m is length of the vehicle, μ = 1.846 × 10^{-5} kg/m·s is dynamic air viscosity. The analyzed freestream velocities are v_∞ = 13.88 m/s, 19.44 m/s and 25 m/s, which corresponds to Re = 3.83 × 10^6, 5.36 × 10^6 and 6.90 × 10^6, respectively.

The velocity profile at the inlet of the computational domain was set uniform in lateral and vertical directions. Turbulence intensity at inlet surface is 0.1 % and the turbulence integral length scale is 0.01 m, which reflects the low-turbulent flow conditions. The physical quantities in the computational domain were initialized using the values at the inlet surface. The computational setup was modeled for stationary viscous air flow, as drag fluctuations for vehicles commonly did not exceed 1 % of the mean value, e.g. (Cadot *et al.*, 2016).

2.4. Governing Equations

The Reynolds-averaged Navier-Stokes (RANS) equations for the incompressible turbulent flow were used together with the shear stress transport (SST) k-ω turbulence model and low Reynolds numbers correction, Menter (1994). The

governing equations of the used RANS model are given as,
a) Continuity equation:

$$\frac{\partial \bar{v}_j}{\partial x_j} = 0\,, \tag{1}$$

b) Momentum equation:

$$\frac{\partial}{\partial x_j}(\bar{v}_j \bar{v}_i) = -\frac{\partial \bar{p}}{\partial x_i} + \frac{\partial}{\partial x_j}\left[\mu\left(\frac{\partial \bar{v}_i}{\partial x_j}+\frac{\partial \bar{v}_j}{\partial x_i}\right) + \right.$$
$$\left. + \mu_t\left(\frac{\partial \bar{v}_i}{\partial x_j}+\frac{\partial \bar{v}_j}{\partial x_i}\right) - \frac{2}{3}\rho \bar{k}\delta_{ij}\right]. \tag{2}$$

The mean air flow velocity is $\bar{v}_i$, the coordinates are x_i, $\bar{p}$ is averaged air pressure, μ_t is turbulent viscosity, $\bar{k}$ is averaged turbulence kinetic energy defined as $\bar{k} = \frac{\overline{v_i' v_i'}}{2}$. Iterative computations started using the first order numerical scheme and finished with the second order upwind numerical scheme. More details on these numerical schemes are available in Ferziger and Perić (2002). The SIMPLE solver was used for the pressure-velocity coupling, while the under-relaxation factors used in the calculations are 0.3 for pressure, 0.7 for momentum, 0.8 for turbulent kinetic energy, 0.8 for specific dissipation rate, and 1 for body forces and turbulent viscosity. The iterative process finished when the residuals of all physical quantities in governing equations were smaller than 10^{-4}, which occured after approximately 1000 iterations of the solver.

The aerodynamic lift and drag forces were analyzed in a form of dimensionless force coefficients,

$$C_D = \frac{F_D}{\frac{1}{2}\rho v_\infty^2 A}\,, \tag{3}$$

$$C_L = \frac{F_L}{\frac{1}{2}\rho v_\infty^2 A}\,, \tag{4}$$

where C_D and C_L are drag and lift force coefficients, respectively. F_D and F_L are aerodynamic drag and lift forces, respectively. A is reference area for aerodynamic force coefficients, calculated as a frontal area of the vehicle perpendicular to the main (x) flow direction; it is equal to 0.87 m^2. The dimensionless pressure coefficient C_p is calculated as,

$$C_p = \frac{p - p_\infty}{\frac{1}{2}\rho v_\infty^2}\,, \tag{5}$$

where p is static pressure, and p_∞ is static pressure of the freestream flow.

3. COMPUTATIONAL RESULTS AND DISCUSSION

3.1. Aerodynamic Force Coefficients

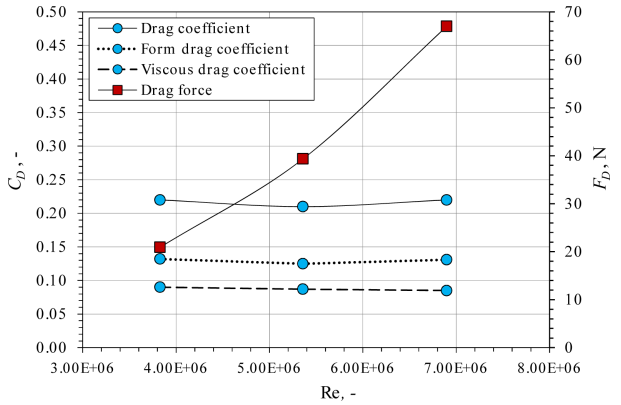

Figure 6. Aerodynamic drag force and drag force coefficients with respect to the Reynolds number of the freestream flow.

The calculated aerodynamic drag force and the respective coefficient are reported for various Reynolds numbers in Figure 6.

The aerodynamic drag force coefficient proves not to be particularly dependent on Reynolds number, as it remains nearly constant when increasing the freestream flow velocity. This is likely due to this particular shape of the vehicle. The obtained drag force coefficient for the solar vehicle is approximately C_D = 0.21. This is considerably smaller than it is common for classic sedan vehicles, e.g. (Katz, 1996).

The form drag coefficient is approximately equal 0.13, while the viscous drag coefficient is 0.08. They are both not particularly dependent on the Reynolds number variations. This yields the contributions of the form drag force and the viscous drag force to the overall drag force of 59 % and 41 %, respectively. On the other hand, for classic passenger vehicles, the viscous drag force contributes negligibly to the overall drag (McBeath, 2011), as the overall drag force is predominantly caused by the pressure distribution on the front and rear surfaces of the vehicle and

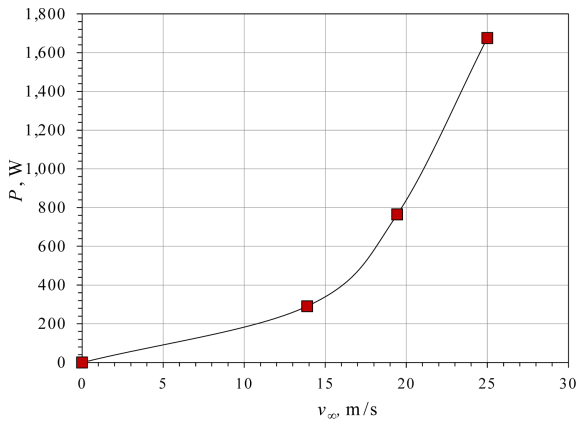

Figure 7. Power required for the vehicle to compensate for the drag force.

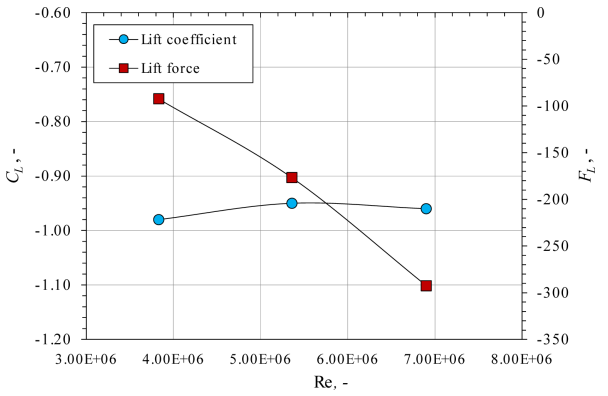

Figure 8. Aerodynamic lift force and lift force coefficient with respect to Reynolds number of the freestream flow.

the flow characteristics in the wake of the vehicles, where flow separation and vortex structures are present. This finding is particularly interesting, as it indicates the viscous drag force considerably gains on importance when addressing aerodynamics of solar vehicles, and this issue merits further work in the future.

The power required for the vehicle to compensate for the drag force is reported in Figure 7 for various vehicle velocities. The power P is calculated as $P = F_D \cdot v_\infty$, while the diagrams are reported for quiescent ambient flow.

The power required to compensate for the aerodynamic drag force is 3rd order polynomial of the vehicle velocity. At 25 m/s (90 km/h), the necessary power to compensate for the aerodynamic drag force is approximately 1.6 kW. This is significantly smaller in comparison with classic passenger vehicles, e.g. approximately 5 kW for classic passenger vehicle (for $C_D = 0.29$ and $A = 2$ m^2).

While the general goal for solar vehicles is not to obtain large downforce, as cornering ability at high speeds is not that important for this type of vehicles, it is neccesary to avoid possible upforce that can destabilize the vehicle. The calculated aerodynamic lift force and the respective coefficient are reported for various Reynolds numbers in Figure 8.

The lift coefficient of the solar vehicle is approximately $C_L = -0.97$, thus indicating the negative aerodynamic lift force, which acts favorably to the dynamic stability of the vehicle. As the negative aerodynamic lift force is obtained for studied vehicle without any additional devices, neither spoilers nor wings are necessary to improve its dynamic behavior, whereas those devices are commonly used for standard vehicles, e.g. (Buljac *et al.*, 2016).

3.2. Pressure Coefficients Distribution

Distribution of the C_p coefficients on the surface of the vehicle body is presented in Figure 9. The results are reported for the top and the bottom surfaces of the vehicle, whereas in the diagram the flow is from left to right.

Distribution of C_p coefficients indicates some

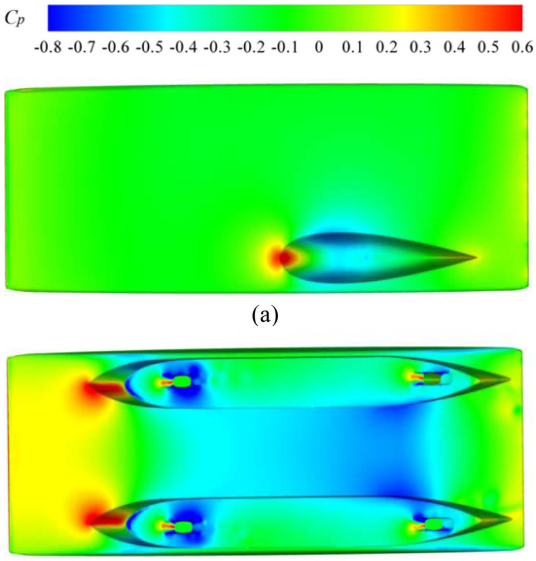

Figure 9. Distribution of C_p coefficients on the surface of the studied solar vehicle: (a) Top view; (b) Bottom view.

characteristic features that are commonly observed in bluff-body aerodynamics. In particular, at the frontal surface of the vehicle, the kinetic energy of the flow predominantly converts into positive pressure, while this phenomenon is particularly exhibited close to the stagnation point.

In general, C_p coefficients are larger on the top of the S_2 shape compared to the lower part of the S_2 shape. Negative C_p coefficients are observed at the lower part of the S_2 shape, as the air is accelerated between the two S_1 shapes. This contributes to the negative lift force of the vehicle and enhances the dynamic stability of the vehicle. The C_p coefficients close to the trailing edge of the vehicle body are close to zero. Intensive pressure drop of the air in the wake of the vehicle is not present. This indicates there is no strong flow separation in the wake of the vehicle. The largest absolute values of the C_p coefficients are obtained in the frontal area of the cockpit canopy and the frontal area of the S_1 shapes. This suggests that these areas are the main sources of the form drag force.

3.3. Shear Stress Distribution

The shear stress acting on the vehicle surface yields the overall viscous drag force (Bakker, 2006). The shear stress distribution on the surface of the vehicle τ_w is presented in Figure 10. In general, large values of the shear stress on the surface indicate an increased contribution to the viscous drag force component, which can be reduced by carefully smoothening a surface roughness of the vehicle.

The relatively larger values of shear stress are generally obtained at surfaces that are more parallel to the freestream flow direction. The largest surface shear stress is obtained on the bottom of the S_2 shape and on the lateral sides of the

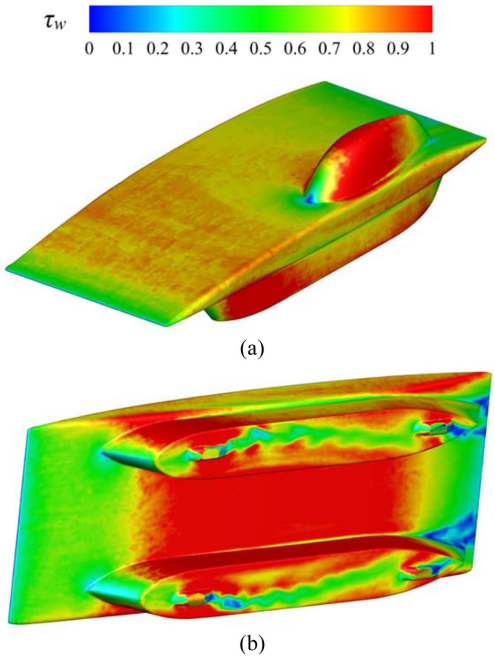

Figure 10. Distribution of the shear stress on the solar vehicle surface: (a) Top view; (b) Bottom view.

S_1 and S_3 shapes. These areas contribute the most to the overall viscous drag force. Relatively low values of the wall shear stress in the wake of the S_1 shapes indicate flow separation, which is further analyzed using the turbulence kinetic energy and vorticity magnitude distributions.

3.4. Velocity Magnitude and Streamlines in Various Planes

As to allow for further analysis of the flow characteristics around the vehicle body, the velocity magnitude field with streamlines is reported for the cockpit canopy plane at $y = 0.7$ m (ground surface is at $y = 0$) in Figure 11. The flow velocity is normalized using the undisturbed freestream flow velocity.

The streamlines of the flow around the NACA0012 airfoil shaped cross-section of the cockpit canopy suggest that the flow remains attached at the cockpit canopy, as the streamlines follow the contour of the canopy. Furthermore, the flow remains attached to the trailing edge of the airfoil. In this way, the aerodynamic drag force of the cockpit canopy is minimized and is predominantly composed of the viscous drag component.

The stagnation zone of the flow can be observed close to the leading edge of the airfoil. In this area, the pressure coefficients are rather large, Figure 9. This phenomenon is caused by relatively large thickness of the airfoil-shape cross section. This can be reduced if the airfoil with smaller thickness is used. However, relatively large thickness of the airfoil is necessary to allow for the driver comfort in the cockpit. These results indicate the favorable properties of the airfoil-shaped cross-section of the cockpit canopy with respect to a reduction in the aerodynamic drag force.

The velocity magnitude field for the plane $z = 0.65$ m is reported in Figure 12. The results show the accelerated flow above the cockpit canopy and beneath the vehicle. The flow generally remains attached to the vehicle body with relatively small separation in the wake of the S_1 shape and in the wake of the rear wheel.

The velocity magnitude field around the vehicle at the height from the ground surface $z = 0.65$ m is reported in Figure 13.

The flow velocity between the two S_1 shapes is generally

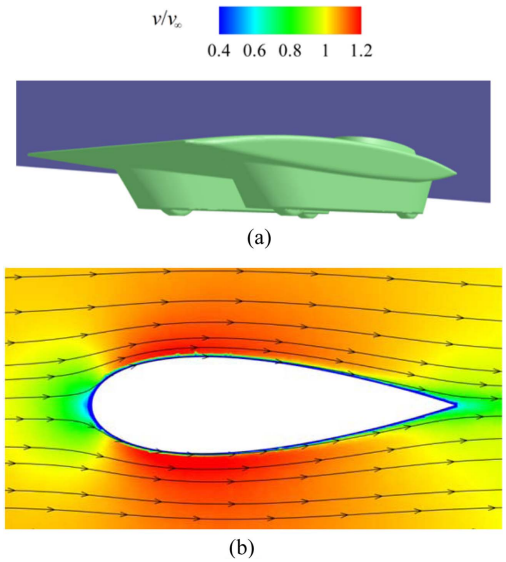

Figure 11. Mean flow velocity with streamlines in the plane $y = 0.7$ m: (a) Plane $y = 0.7$ m; (b) Velocity distribution.

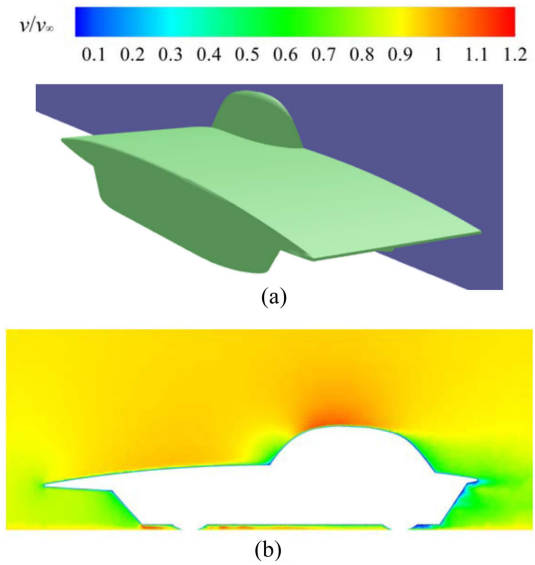

Figure 12. Velocity magnitude around the vehicle body in the plane $z = 0.65$ m: (a) Plane $z = 0.65$ m; (b) Velocity distribution.

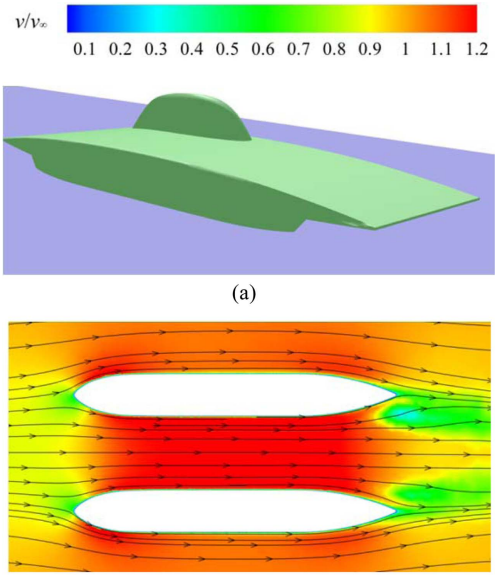

Figure 13. Velocity magnitude around the vehicle body in the plane y = 0.3 m: (a) Plane y = 0.3 m; (b) Velocity distribution.

increased with respect to the freestream flow. The air gradually decelerates towards the trailing edge of the S_1 shapes. The flow remains attached in the wake of the S_1

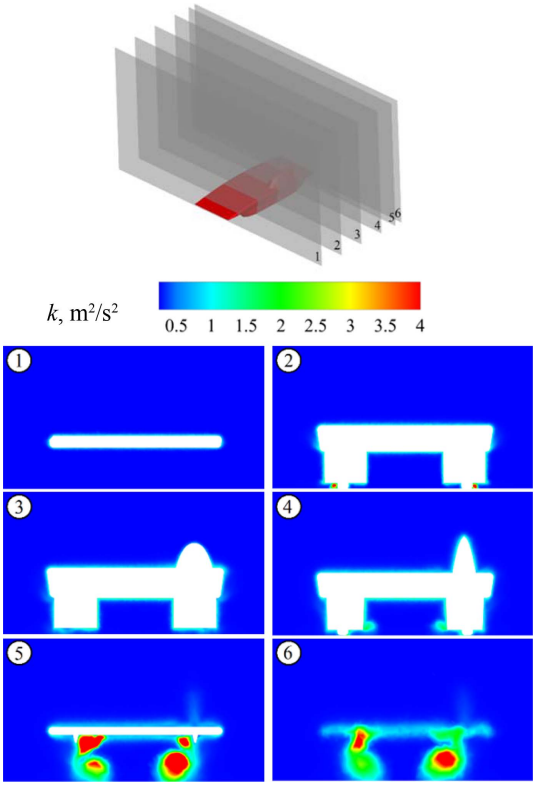

Figure 14. Distribution of the turbulence kinetic energy k in various planes around the solar vehicle.

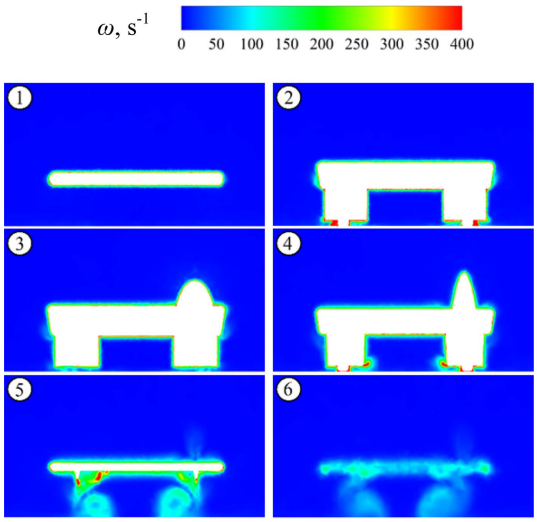

Figure 15. Vorticity magnitude ω in various planes around the solar vehicle.

shapes.

As to allow for additional analysis of the flow structures around the solar vehicle body, a distribution of the turbulence kinetic energy k in various planes around the vehicle is reported in Figure 14 for v_∞ = 14 m/s.

While the turbulence kinetic energy is relatively small around the front part of the vehicle, relatively large values can be observed in the wake of the wheels, S_1 shapes, and in the wake of the vehicle. The cockpit canopy does not induce any significant increase in the turbulence kinetic energy as observed in planes 5 and 6. The cockpit canopy, however, influences the distribution of the turbulence kinetic energy in the wake of the S_1 shapes (plane 5) and in the wake of the vehicle (plane 6), as the distribution is not symmetric with respect to the center of the vehicle. This is possibly due to a suction of the flow from the outer side of the cockpit canopy (right-hand side looking from the flow direction) towards the S_1 shape, which creates a vortex on the edge of the S_2 shape.

The vorticity magnitude ω of the flow for the planes 1 ~

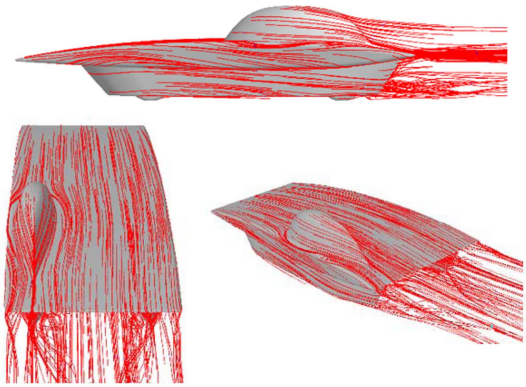

Figure 16. Flow streamlines around the solar vehicle.

6 is reported in Figure 15 for v_∞ = 14 m/s.

Increased vorticity magnitude can be observed in the wake of the S_1 shapes (plane 5) and in the wake of the vehicle (plane 6). The results in the plane 5 suggest that two large vortices formed close to the ground in between two S_1 shapes, while they gradually vanished towards the plane 6. These vortices likely developed from the inside bottom tip of the S1 shapes, as can be observed in plane 4. These results are complemented with the flow streamlines around the solar vehicle reported in Figure 16.

The flow streamlines suggest that no vortices are present in the wake of the cockpit canopy, while the vortices formed in the wake of the S_2 shape edges, and close to the ground in between two S_1 shapes, as indicated in Figure 15. The side view shows the streamlines that developed from the outer side of the cockpit canopy (right-hand side looking from the flow direction) towards the S_1 shape.

4. CONCLUSION

Aerodynamic forces and flow characteristics were analyzed for a solar road vehicle with a streamlined body. For this purpose, a computational fluid dynamics model was developed. Computations were carried out for the steady viscous flow using the Reynolds-averaged Navier-Stokes equations and the k-ω turbulence model. The results indicate several important findings. A contribution of the viscous drag force to the overall drag force is considerably larger (41 %) than it is the case for the standard passenger road vehicles. This indicates a necessity for a careful consideration of the vehicle surface roughness, i.e. it is necessary to design it as smooth as possible to decrease an adverse increase in fuel consumption. Surface pressure distribution patterns indicate a favorable aerodynamic design of this vehicle. In particular, larger pressure coefficients were obtained on the top of the vehicle body as compared to the bottom surface, which combined contributes to an increase in favorable downforce thus enhancing the vehicle traction ability. The airfoil-shaped cross section of the cockpit canopy proves to have favorable properties with respect to a reduction in the aerodynamic drag force.

ACKNOWLEDGEMENT–This study is a part of the 'Istraživanje i razvoj solarnog električnog automobila' project of the Faculty of Electrical Engineering, University of Osijek, Croatia, which support is gratefully acknowledged.

REFERENCES

Amann, C. A. (1994). Private vehicles for personal transportation. *Int. J. Vehicle Design* **14**, **5-6**, 399–430.

Bakker, A. (2006). Applied Computational Fluid Dynamics. Lecture 11 – Boundary Layers and Separation.

Barros, D., Borée, J., Noack, B. R., Spohn, A. and Ruiz, T. (2016). Bluff body drag manipulation using pulsed jets and Coanda effect. *J. Fluid Mechanics*, **805**, 422–459.

Birnie, D. P. (2016). Analysis of energy capture by vehicle solar roofs in conjunction with workplace plug-in charging. *Solar Energy*, **125**, 219–226.

Buljac, A., Džijan, I., Korade, I., Krizmanić, S. and Kozmar, H. (2016). Automobile aerodynamics influenced by airfoil-shaped rear wing. *Int. J. Automotive Technology* **17**, **3**, 377–385.

Cadot, O., Courbois, A., Ricot, D., Ruiz, T., Harambat, F. and Herbert, V. (2016). Characterisations of force and pressure fluctuations of real vehicles. *Int. J. Engineering Systems Modelling and Simulation* **8**, **2**, 99–105.

Doig, G. and Beves, C. (2014). Aerodynamic design and development of the Sunswift IV solar racing car. *Int. J. Vehicle Design* **66**, **2**, 144–167.

Elofsson, P. and Bannister, M. (2002). Drag reduction mechanisms due to moving ground and wheel rotation in passenger cars. *SAE Paper No*. 2002-01-0531.

Ferziger, J. H. and Perić, M. (2002). *Computational Methods for Fluid Dynamics*. Spriger-Verlag Berlin Heidelberg. Heidelberg, Germany.

Gregory, N. and O'Reilly, C. L. (1970). *Low-speed Aerodynamic Characteristics of NACA 0012 Aerofoil Section, Including the Effects of Upper-surface Roughness Simulating Hoar Frost*. Research Council. London, UK.

Huminic, A. and Huminic, G. (2017). Aerodynamic study of a generic car model with wheels and underbody diffuser. *Int. J. Automotive Technology* **18**, **3**, 397–404.

Kang, S. O., Jun, S. O., Park, H. I., Song, K. S., Kee, J. D., Kim, K. H. and Lee, D. H. (2012). Actively translating a rear diffuser device for the aerodynamic drag reduction of a passenger car. *Int. J. Automotive Technology* **13**, **4**, 583–592.

Katz, J. (1996). *Race Car Aerodynamics.* Bentley Publishers. Cambridge, UK.

Khaled, M., El Hage, H., Harambat, F. and Peerhossaini, H. (2012). Some innovative concepts for car drag reduction: A parametric analysis of aerodynamic forces on a simplified body. *J. Wind Engineering and Industrial Aerodynamics*, **107-108**, 36–47.

McBeath, S. (2011). *Competition Car Aerodynamics*. Haynes Publishing. Bristol, UK.

McNally, J., Fernandez, E., Robertson, G., Kumar, R.,Taira, K., Alvi, F., Yamaguchi, Y. and Murayama, K. (2015). Drag reduction on a flat-back ground vehicle with active flow control. *J. Wind Engineering and Industrial Aerodynamics*, **145**, 292–303.

Menter, F. R. (1994). Two-equation eddy-viscosity turbulence models for engineering applications. *AIAA Journal* **32**, **8**, 1598–1605.

Rao, G. S., Rao, G. K., Murthy, G. R. K. and Obulesh, Y. (2009). Power management policies and control of hybrid electric vehicle. *Int. J. Renewable Energy Technology* **1**, **1**, 101–113.

Saber, A. Y. and Venayagamoorthy, G. K. (2011). Plug-in

vehicles and renewable energy sources for cost and emission reductions. *IEEE Trans. Industrial Electronics* **58**, **4**, 1229–1238.

Salim, S. M. and Cheah, S. C. (2009). Wall y^+ strategy for dealing with wall-bounded turbulent flows. *Proc. Int. MultiConf. Engineerings and Computer Science*, Hong Kong.

Sharma, D., Gaur, P. and Mittal, A. P. (2013). Energy management system for a PV assisted conventional vehicle. *Int. J. Energy Technology and Policy* **9**, **2**, 144–159.

Song, K. S., Kang, S. O., Jun, S. O., Park, H. I., Kee, J. D., Kim, K. H. and Lee, D. H. (2012). Aerodynamic design optimization of rear body shapes of a sedan for drag reduction. *Int. J. Automotive Technology* **13**, **6**, 905–914.

Taha, Z., Passarella, R., Sugiyono, Nasrudin, A. R., Jamali, M. S. and Aznijar, A. Y. (2011). CFD analysis for Merdeka 2 solar vehicle. *Advanced Science Letters* **4**, **8-10**, 2807–2811.

Vinnichenko, N. S., Uvarov, A. V., Znamenskaya, I. A., Herchang, A. Y. and Wang, T. (2014). Solar car aerodynamic design for optimal cooling and high efficiency. *Solar Energy*, **103**, 183–190.

West, G. S. and Apelt, C. J. (1982). The effects of tunnel blockage and aspect ratio on the mean flow past a circular cylinder with Reynolds numbers between 10^4 and 10^5. *J. Fluid Mechanics*, **114**, 361–377.